INORGANIC CHEMISTRY
FRONTIERS

CHINESE CHEMICAL SOCIETY

ROYAL SOCIETY OF CHEMISTRY

RESEARCH ARTICLE

View Article Online
View Journal | View Issue

Cite this: *Inorg. Chem. Front.*, 2024, **11**, 3296

Homochiral Dy_2 single-molecule magnets with strong magneto-optical Faraday effects and strong third-harmonic generation†

Cai-Ming Liu, *[a] Rong Sun,[b] Xiang Hao,[a] Xi-Li Li [c] and Bing-Wu Wang *[b]

Four pairs of homochiral Dy_2 complexes were directionally prepared using homochiral β-diketone ligands {D-Htfc/L-Htfc = (+)/(−)-3-trifluoroacetyl camphor, D-Hpfc/L-Hpfc = 3-(perfluorobutyryl)-(+)/(−)-camphor} and hydrazone Schiff base bridging ligands {H_2L1 = (*E*)-*N*′-(2-hydroxy-3-methoxybenzylidene)pyrazine-2-carbohydrazide, H_2L2 = (*E*)-*N*′-(2-hydroxy-3-methoxybenzylidene)nicotinohydrazide} at room temperature: $[Dy_2(\text{D-tfc/L-tfc})_2(\text{L1})_2(H_2O)_2]\cdot 2DMF$ (***D*-1**/***L*-1**), $[Dy_2(\text{D-tfc/L-tfc})_2(\text{L2})_2(H_2O)_2]\cdot 2DMF$ (***D*-2**/***L*-2**), $[Dy_2(\text{D-pfc/L-pfc})_2(\text{L1})_2(DMF)_2]$ (***D*-3**/***L*-3**), and $[Dy_2(\text{D-pfc/L-pfc})_2(\text{L2})_2(H_2O)_2]\cdot 2DMF$ (***D*-4**/***L*-4**). These enantiomers show intramolecular ferromagnetic interactions between Dy^{3+} ions and exhibit good single-molecule magnet (SMM) properties at a zero dc field, with U_{eff}/k values of 47.6 K, 152.2 K, 173.8 K and 116.2 K for ***D*-1**, ***D*-2**, ***D*-3** and ***D*-4**, respectively. These magnetic properties were explained with *ab initio* calculations. The magnetic circular dichroism (MCD) investigation revealed that these four pairs of enantiomers have strong magneto-optical Faraday effects. Besides the second harmonic generation (SHG), they exhibit surprisingly strong third harmonic generation (THG). Notably, the magnetic properties, magneto-optical properties and nonlinear optical properties of such homochiral SMMs can be adjusted by the functional groups on the ligands. Among them, ***D*-1**/***L*-1** has the potential for applications in magneto-optical and/or nonlinear optical materials or devices due to its strongest THG intensity (661.8 × α-SiO_2) and strongest magneto-optical Faraday effect.

Received 18th March 2024,
Accepted 15th April 2024

DOI: 10.1039/d4qi00691g

rsc.li/frontiers-inorganic

Introduction

Chiral single-molecule magnets (SMMs) have attracted increasing attention as a special class of nanomagnets,[1–28] and the advantage is that they can be endowed with many new properties closely related to chirality, such as ferroelectrics,[1,8–12] second-order nonlinear optics,[13–17] circularly polarized luminescence,[4,18–22] magnetic circular dichroism (MCD),[23–28] and magnetochiral dichroism (MChD),[2,4,23] so as to become nanoscale multifunctional molecular materials. Therefore, SMMs are no longer limited to being used as high-density information storage materials[29] after gaining chirality; for example, chiral SMMs with a strong MChD effect have the potential for optical readout of magnetically stored data.[2] If chiral SMMs have a strong magneto-optical Faraday effect, they are expected to be used in optical fiber technology such as magneto-optical switches, isolators or sensors, and photocurrent transformers.[23–28] However, so far, only a few chiral SMMs with strong magneto-optical Faraday effects have been explored.[23–28] The reason is that the construction of chiral SMMs is a difficult task in itself,[30] and a strong Faraday effect is also difficult to achieve.[23–28] Interestingly, recent studies have shown that some homochiral SMMs exhibit third-harmonic generation (THG) in addition to second-harmonic gene-

---

[a] *Beijing National Laboratory for Molecular Sciences, CAS Key Laboratory for Organic Solids, Institute of Chemistry, Chinese Academy of Sciences, Beijing 100190, China. E-mail: cmliu@iccas.ac.cn*

[b] *State Key Laboratory of Rare Earth Materials Chemistry and Applications, College of Chemistry and Molecular Engineering, Peking University, Beijing 100871, China. E-mail: wangbw@pku.edu.cn*

[c] *Henan Provincial Key Laboratory of Surface and Interface Science, Zhengzhou University of Light Industry, Zhengzhou 450002, China*

† Electronic supplementary information (ESI) available: Crystal data and structural refinement parameters for ***D*-1**/***L*-1**, ***D*-2**/***L*-2**, ***D*-3**/***L*-3** and ***D*-4**/***L*-4**; continuous shape measures calculation for Dy(III) ions in ***D*-1**, ***D*-2**, ***D*-3** and ***D*-4**; M *versus* H/T and hysteresis loop plots for ***D*-1**, ***D*-2**, ***D*-3** and ***D*-4**; the ac magnetic susceptibility of ***D*-1**, ***D*-2**, ***D*-3** and ***D*-4** at 1500 Oe; calculated energy levels and $g(g_x, g_y, g_z)$ tensors of the lowest Kramers doublets (KDs) of individual Dy(III) fragments for ***D*-1**, ***D*-2**, ***D*-3** and ***D*-4**; wave functions with definite projection of the total moment $|m_J>$ for the lowest three Kramers doublets (KDs) of individual Dy^{3+} fragments in ***D*-1**, ***D*-2**, ***D*-3** and ***D*-4**; plots of χT *versus* T of ***D*-1**, ***D*-2**, ***D*-3** and ***D*-4** with the simulated results; the orientations of the easy axis of the KDs on Dy^{3+} for ***D*-1**, ***D*-2**, ***D*-3** and ***D*-4**; MCD spectra and the wavelength-dependent g_{MCD} curves of ***D*-1**/***L*-1**, ***D*-2**/***L*-2**, ***D*-3**/***L*-3** and ***D*-4**/***L*-4**; SHG spectra of the crystalline samples of ***D*-1**, ***D*-2**, ***D*-3**, ***D*-4** and KDP. CCDC 2308016–2308023. For ESI and crystallographic data in CIF or other electronic format, see DOI: **https://doi.org/10.1039/d4qi00691g**

ration (SHG), but no magneto-optical Faraday effects are reported,[15,16] while nonlinear optical materials generally play a key role in optical communications, laser manufacturing, therapeutics, and military applications.[31–34]

Lanthanide(III) ions have become the best components for the construction of SMMs due to their large spin ground states and magnetic anisotropy.[35–37] At present, SMMs with the largest energy barrier values and the highest blocking temperatures are based on lanthanide(III) mononuclear complexes,[3,38–42] and the main advantage is that the magnetic axis of a single lanthanide(III) ion is easy to maintain.[43] However, for lanthanide(III) complexes, increasing the magnetic dipole moments in their ground and excited states is beneficial for enhancing their MCD effects.[44] Therefore, it is necessary to construct chiral lanthanide(III) multinuclear complexes to obtain chiral SMMs with strong Faraday effects. Chiral lanthanide(III) SMMs with ferromagnetic coupling are of particular interest, since the cumulative spin ground-state values can be obtained and the quantum tunnelling effect can be suppressed.[24] However, the magnetic exchange of 4f electrons from different lanthanide(III) ions is generally difficult, and weak antiferromagnetic interactions predominate. In this study, we focused on the directional construction of ferromagnetically coupled dysprosium(III) binuclear SMMs using homochiral β-diketone terminal ligands (D-Htfc/L-Htfc, D-Hpfc/L-Hpfc, Scheme 1) and hydrazone Schiff base bridging ligands (H_2L1 and H_2L2, Scheme 1). Herein, we report the precise preparation, crystal structures, magnetic behaviours, magneto-optical Faraday effects and nonlinear optical properties of four pairs of homochiral Dy_2 complexes, $[Dy_2(\text{D-tfc/L-tfc})_2(L1)_2(H_2O)_2]\cdot 2DMF$ {***D*-1/*L*-1**, H_2L1 = (*E*)-*N'*-(2-hydroxy-3-methoxybenzylidene) pyrazine-2-carbohydrazide, D-Htfc/L-Htfc = (+)/(−)-3-trifluoroacetyl camphor}, $[Dy_2(\text{D-tfc/L-tfc})_2(L2)_2(H_2O)_2]\cdot 2DMF$ {***D*-2/*L*-2**, H_2L2 = (*E*)-*N'*-(2-hydroxy-3-methoxybenzylidene)nicotinohydrazide}, $[Dy_2(\text{D-pfc/L-pfc})_2(L1)_2(DMF)_2]$ {***D*-3/*L*-3**, D-Hpfc/L-Hpfc = 3-(perfluorobutyryl)-(+)/(−)-camphor}, and $[Dy_2(\text{D-pfc/L-pfc})_2(L2)_2(H_2O)_2]\cdot 2DMF$(***D*-4/*L*-4**). These four pairs of enantiomers are zero-field SMMs and show strong magneto-optical Faraday effects. In addition to having second-order nonlinear optical responses, these four enantiomers exhibit very strong third-order nonlinear optical responses, depending on the functional groups on the ligands.

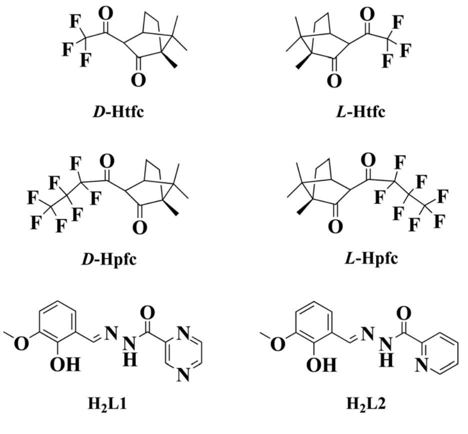

Scheme 1 D-Htfc/L-Htfc, D-Hpfc/L-Hpfc, H_2L1 and H_2L2.

Experimental

Materials and methods

All analytically pure chemicals and solvents are commercially available. H_2L1 and H_2L2 were synthesized by the methods reported in the literature.[45,46]

Elemental analyses were performed on a Thermo FlashSmart elemental analyzer. Infrared spectra were recorded on a Bruker VERTEX 70v spectrophotometer with pressed KBr pellets. Circular dichroism (CD) spectra and magnetic circular dichroism (MCD) spectra were recorded using a Jasco J-1700, with a permanent magnet (+1.6 T or −1.6 T) and a 5 mm optical path. Magnetic properties were analysed on a Quantum Design MPMS-XL5 (SQUID) magnetometer. The diamagnetism of all constituent atoms was corrected using Pascal's constant.

Preparation of *D*-1 and *L*-1

0.25 mmol of H_2L1, 0.25 mmol of $Dy(CF_3SO_3)_3$ and 0.75 mmol of $LiOH\cdot H_2O$ were added successively to 0. 25 mmol of (+)/(−)-3-trifluoroacetyl camphor in 5 mL of DMF. After stirring for 60 minutes, yellow turbidity appeared, and the solution became clear after adding 30 ml of CH_2Cl_2 to the reaction mixture; after another 23 hours of stirring, a yellow solution formed, which was filtered and transferred to a beaker, where crystals grew by slowly volatilizing the solvent. After several days, brown single crystals of ***D*-1/*L*-1** were harvested. Yield: about 50% based on Dy.

Elemental analysis calcd (%) for $C_{56}H_{66}F_6N_{10}O_{14}Dy_2$ (***D*-1**): C, 43.61; H, 4.31; N, 9.08; found: C, 43.55; H, 4.35; N, 9.01. IR (KBr, cm^{-1}): 3357 (w, br), 3287 (w, br), 3084(w), 2954(w), 2832(w), 1642(s), 1597(m), 1556(m), 1521(w), 1474(w), 1443(m), 1413(w), 1390(w), 1331(m), 1298(w), 1267(w), 1226(m), 1221(w), 1182(w), 1155(w), 1131(m), 1103(w), 1080(w), 1055(w), 1034(w), 1011(w), 967(w), 919(w), 875(w), 858(w), 806(w), 776(w), 746(m), 709(w), 683(w), 665(w), 645(w), 595(w), 554(w), 530(w), 488(w), 430(w).

Elemental analysis calcd (%) for $C_{56}H_{66}F_6N_{10}O_{14}Dy_2$ (***L*-1**): C, 43.61; H, 4.31; N, 9.08; found: C, 43.65; H, 4.34; N, 9.03. IR (KBr, cm^{-1}): 3372 (w, br), 3290 (w, br), 3084(w), 2954(w), 2832(w), 1666(s), 1597(m), 1555(m), 1520(w), 1474(w), 1443(m), 1413(w), 1390(w), 1331(m), 1298(w), 1267(w), 1226(m), 1221(w), 1182(w), 1155(w), 1131(m), 1103(w), 1080(w), 1055(w), 1034(w), 1011(w), 967(w), 919(w), 875(w), 858(w), 806(w), 776(w), 746(m), 709(w), 683(w), 665(w), 645(w), 595(w), 555(w), 530(w), 488(w), 430(w).

Preparation of *D*-2 and *L*-2

***D*-2** and ***L*-2** were synthesized using a similar reaction pathway to ***D*-1** and ***L*-1**, but with H_2L1 replaced with H_2L2. Yellow single crystals of ***D*-2/*L*-2** were obtained. Yield: 45% based on Dy.

Elemental analysis calcd (%) for $C_{58}H_{68}Dy_2F_6N_8O_{14}$ (**_D_-2**): C, 45.23; H, 4.45; N, 7.28; found: C, 45.17; H, 4.50; N, 7.23. IR (KBr, cm^{-1}): 3359 (w, br), 3070(w), 2956(w), 2832(w), 1669(vs), 1660(s), 1555(s), 1479(m), 1443(m), 1413(w), 1390(w), 1339(w), 1324(w), 1299(w), 1267(w), 1226(s), 1200(m), 1184(m), 1159(w), 1125(m), 1103(w), 1079(w), 1048(w), 1017(w), 966(w), 918(w), 858(w), 806(w), 747(m), 714(w), 692(w), 665(w), 640(w), 595(w), 554(w), 531(w), 477(w), 422(w).

Elemental analysis calcd (%) for $C_{58}H_{68}Dy_2F_6N_8O_{14}$ (**_L_-2**): C, 45.23; H, 4.45; N, 7.28; found: C, 45.27; H, 4.51; N, 7.21. IR (KBr, cm^{-1}): 3353 (w, br), 3069(w), 2958(w), 2832(w), 1669(vs), 1661(s), 1555(s), 1479(m), 1444(m), 1413(w), 1390(w), 1340(w), 1325(w), 1299(w), 1268(w), 1226(s), 1201(m), 1185(m), 1159(w), 1126(m), 1104(w), 1079(w), 1050(w), 1017(w), 968(w), 918(w), 859(w), 808(w), 747(m), 714(w), 692(w), 666(w), 641(w), 596(w), 554(w), 532(w), 477(w), 422(w).

Preparation of _D_-3 and _L_-3

_D_-3 and **_L_-3** were synthesized using a similar reaction pathway to **_D_-1** and **_L_-1**, but with D-Htfc/L-Htfc replaced with D-Hpfc/L-Hpfc. Brown single crystals of **_D_-3**/**_L_-3** were obtained. Yield: 55% based on Dy.

Elemental analysis calcd (%) for $C_{60}H_{62}Dy_2F_{14}N_{10}O_{12}$ (**_D_-3**): C, 42.24; H, 3.66; N, 8.21; found: C, 42.29; H, 3.71; N, 8.15. IR (KBr, cm^{-1}): 3406 (m, br), 2995(w), 2962(m), 2931(w), 2833(w), 1663(s), 1603(s), 1558(m), 1535(m), 1475(m), 1445(m), 1419(w), 1385(w), 1336(m), 1216(s), 1180(m), 1057(w), 1036(w), 952(w), 923(w), 897(w), 859(w), 814(w), 780(w), 745(m), 637(w), 617(w), 598(w), 535(w), 491(w), 432(w).

Elemental analysis calcd (%) for $C_{60}H_{62}Dy_2F_{14}N_{10}O_{12}$ (**_L_-3**): C, 42.24; H, 3.66; N, 8.21; found: C, 42.21; H, 3.72; N, 8.16. IR (KBr, cm^{-1}): 3411 (m, br), 2996(w), 2962(m), 2930(w), 2833(w), 1663(s), 1603(s), 1558(m), 1535(m), 1475(m), 1445(m), 1419(w), 1386(w), 1335(m), 1216(s), 1181(m), 1054(w), 1035(w), 1011(w), 952(w), 923(w), 897(w), 859(w), 814(w), 781(w), 745(m), 636(w), 616(w), 598(w), 534(w), 491(w), 432(w).

Preparation of _D_-4 and _L_-4

_D_-4 and **_L_-4** were synthesized using a similar reaction pathway to **_D_-1** and **_L_-1**, but with H_2L1 replaced with H_2L2 and D-Htfc/L-Htfc replaced with D-Hpfc/L-Hpfc. Yellow-green single crystals of **_D_-4**/**_L_-4** were obtained. Yield: 65% based on Dy.

Elemental analysis calcd (%) for $C_{62}H_{69}Dy_2F_{14}N_8O_{14}$ (**_D_-4**): C, 42.77; H, 3.99; N, 6.44; found: C, 42.73; H, 4.02; N, 6.37. IR (KBr, cm^{-1}): 3392(w, br), 3055(w), 2962(m), 2932(w), 2836(w), 1667(s), 1602(s), 1555(m), 1537(m), 1480(m), 1446(m), 1393(w), 1342(m), 1298(w), 1233(s), 1213(s), 1179(m), 1108(m), 1079(w), 1044(w), 1019(w), 971(w), 951(w), 919(w), 896(w), 860(w), 811(w), 781(w), 740(m), 692(w), 667(w), 636(w), 613(w), 596(w), 533(w), 486(w), 420(w).

Elemental analysis calcd (%) for $C_{62}H_{69}Dy_2F_{14}N_8O_{14}$ (**_L_-4**): C, 42.77; H, 3.99; N, 6.44; found: C, 42.81 H, 4.04; N, 6.39. IR (KBr, cm^{-1}): 3397(w, br), 3055(w), 2962(m), 2933(w), 2836(w), 1666(s), 1603(s), 1555(m), 1537(m), 1480(m), 1446(m), 1391(w), 1342(m), 1298(w), 1233(s), 1214(s), 1179(m), 1110(m), 1079(w), 1044(w), 1019(w), 971(w), 951(w), 920(w), 8976(w), 861(w), 811(w), 781(w), 741(m), 692(w), 668(w), 637(w), 614(w), 596(w), 534(w), 487(w), 419(w).

Crystallography

The collection of X-ray single crystal diffraction data for the four pairs of enantiomers was carried out using a Rigaku MM007HF diffractometer with Mo-Kα radiation ($\lambda = 0.71073$ Å) at 170 K. All eight crystal structures were solved using the olex2.solve structure solution program and refined with the ShelXL-2015 refinement package. All non-hydrogen atoms were refined anisotropically, and all hydrogen atoms were treated as riding atoms. Crystallographic data are summarized in Table S1.†

Nonlinear optical response measurements

An ultrafast fibre laser (NPI Lasers, Rainbow 1550 OEM) was used as the excitation source to output 100 fs pulses at 1550 nm with a repetition rate of 80 MHz. This laser beam was then focused using an aspheric lens with a numerical aperture of 0.8, resulting in a laser spot with a beam waist radius of 2 μm. The spectra of SHG and THG were recorded using a cooled fibre optic spectrometer (Ideaoptics, NOVA). For comparison, the same integration time ($T_{\text{int}} = 0.5$ s) was used to obtain SHG and THG signals for the sample and reference materials. Their SHG and THG mappings were monitored by integrating SHG and THG spectra at different locations over integration ranges of 750–800 nm for SHG and 500–550 nm for THG.

Results and discussion

Synthesis

The hydrazone Schiff base ligands H_2L1 and H_2L2, which are formed by the condensation of o-vanillin and pyrazine-2-carbohydrazide or 2-pyridinecarbohydrazide, had been used to construct several ferromagnetic coupling Dy_2 SMMs before,[45–49] and some of them even used the β-diketone ligand acetylacetone as the terminal ligand;[50] however, all these ferromagnetic coupling Dy_2 SMMs are achiral. Very recently, we used homochiral β-diketone ligands D-Htfc/L-Htfc and other Schiff base ligands to construct two pairs of homochiral Dy_4 SMMs,[27] but they did not exhibit ferromagnetic coupling. In this study, we aim to utilize D-Htfc/L-Htfc and D-Hpfc/L-Hpfc as the terminal ligands as well as H_2L1 and H_2L2 as the bridging ligands to directionally construct homochiral ferromagnetic coupling Dy_2 SMMs. The reaction of H_2L1/H_2L2, D-Htfc/L-Htfc, $Dy(CF_3SO_3)_3$ and $LiOH·H_2O$ in a DMF–CH_2Cl_2 mixed solvent at room temperature yielded **_D_-1**/**_L_-1** and **_D_-2**/**_L_-2**, while the reaction of H_2L1/H_2L2, D-Hpfc/L-Hpfc, $Dy(CF_3SO_3)_3$ and $LiOH·H_2O$ in a DMF–CH_2Cl_2 mixed solvent at room temperature yielded **_D_-3**/**_L_-3** and **_D_-4**/**_L_-4**. Notably, these reactions are directed and can be achieved repeatedly. Additionally, these reactions are conducted at room temperature, which may avoid racemization of the product using the high-temperature hydrothermal technique.

Crystal structures

The single crystal structure analyses showed that the Flack values of the four pairs of homochiral isomers are close to zero (Table S1†), which verify the chiral nature of these enantiomers. Because the enantiomers are structurally similar, we focus on describing the crystal structures of ***D*-1**, ***D*-2**, ***D*-3** and ***D*-4** only. ***D*-1** and ***L*-1** are crystallized in the chiral space group $P2_1$. As shown in Fig. 1a, ***D*-1** is a chiral dysprosium(III) dinuclear complex, in which two Dy^{3+} cations are chelated in opposite directions by two $L1^{2-}$ ligands of an approximate plane, while D-tfc$^-$ anions and coordination water molecules are coordinated to the Dy^{3+} cations as terminal ligands. Notably, the coordinated D-tfc$^-$ anions from different Dy^{3+} cations are located on the upper and lower sides of the $[Dy_2(L1)_2]$ approximate plane, as are the coordinated water molecules. A similar arrangement was observed in $[RE_2(L2)_2(acac)_2(H_2O)_2]\cdot$i-PrOH (RE = Y, Eu, Dy, Ho, Er and Yb; Hacac = acetylacetone) and $[Dy_2(L2)_2(acac)_2(EtOH)_2]$.[50] The Dy1⋯Dy2 distance is 3.902 Å. Each Dy^{3+} ion has the $[O_6N_2]$ coordination configuration, which is coordinated by one $N_{pyrazine}$ atom and one $O_{carbonyl}$ atom in one $L1^{2-}$ ligand, one O_{phenol} atom, one N_{imine} atom and one $O_{carbonyl}$ atom in the other $L1^{2-}$ ligand, two O atoms in the D-tfc$^-$ anion, and one O_{water} atom. Further analysis using the Shape software[51] showed that the coordination configurations of Dy1 and Dy2 are the triangular dodecahedron, with CShM values of 1.726 and 1.487, respectively (Table S2†). The crystal structure of ***L*-1** (Fig. 1b) is very similar to that of ***D*-1** (Fig. 1a), but ***L*-1** is mirror-symmetrical to ***D*-1** (Fig. 1).

***D*-2** and ***L*-2** are also crystallized in the chiral space group $P2_1$. As shown in Fig. 2a, the crystal structure of ***D*-2** is similar to that of ***D*-1** (Fig. 1a), except that the bridging ligand changes from $L1^{2-}$ to $L2^{2-}$. Two Dy^{3+} cations in ***D*-2** are chelated in opposite directions by two $L2^{2-}$ ligands of an approximate plane, and the D-tfc$^-$ terminal ligands attached to Dy1 or Dy2 are located on two sides of the $[Dy_2(L2)_2]$ approximate plane, as are the coordination water molecules. The Dy1⋯Dy2 distance of 3.899 Å in ***D*-2** is comparable to that in ***D*-1** (3.902 Å). Each Dy^{3+} ion in ***D*-2** also has a $[O_6N_2]$ coordination configuration, which is coordinated by one $N_{pyrazine}$ atom and one $O_{carbonyl}$ atom in one $L2^{2-}$ anion, one O_{phenol} atom, one N_{imine} atom and one $O_{carbonyl}$ atom in the other $L2^{2-}$ anion, two O atoms from the D-tfc$^-$ anion, and one O_{water} atom. The Shape software analysis[51] showed that the coordination configurations of Dy1 and Dy2 in ***D*-2** are the triangular dodecahedron, with CShM values of 1.784 and 1.530, respectively (Table S3†). The crystal structure of ***L*-2** (Fig. 2b) is very similar to that of ***D*-2** (Fig. 2a), but ***L*-2** is mirror-symmetrical to ***D*-2** (Fig. 2).

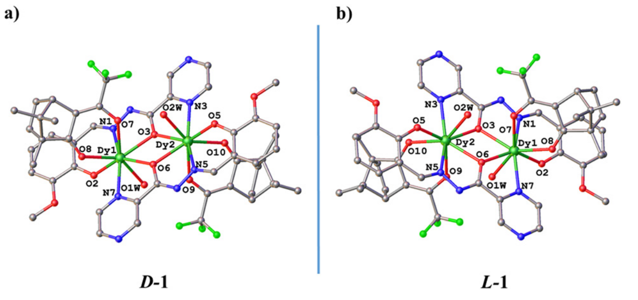

Fig. 1 Crystal structures of ***D*-1(a)** and ***L*-1(b)**; all H atoms and solvent molecules are omitted for clarity.

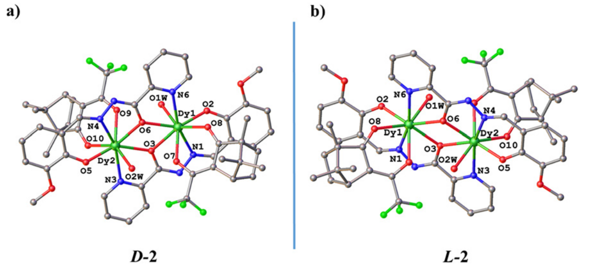

Fig. 2 Crystal structures of ***D*-2(a)** and ***L*-2(b)**; all H atoms and solvent molecules are omitted for clarity.

***D*-3** and ***L*-3** are crystallized in a different chiral space group $P1$ rather than $P2_1$. Correspondingly, the structure of ***D*-3** contains two crystallographically independent molecules instead of one. As shown in Fig. 3a, the crystal structure of ***D*-3** is similar to that of ***D*-1** (Fig. 1a), except that the terminal ligands change from D-tfc$^-$ to D-pfc$^-$ and H_2O to DMF. In each crystal-independent molecule, two Dy^{3+} cations are chelated by two approximately planar $L1^{2-}$ ligands in opposite directions, and the two D-pfc$^-$ terminal ligands from two different Dy^{3+} cations are located on the upper and lower sides of the approximately planar $[Dy_2(L1)_2]$, as are the coordinated DMF molecules. The Dy1⋯Dy2 distance of 3.887 Å is a little shorter than the Dy3⋯Dy4 distance of 3.906 Å. Each Dy^{3+} ion in ***D*-3** also has a $[O_6N_2]$ coordination configuration, which is coordinated by one $N_{pyrazine}$ atom and one $O_{carbonyl}$ atom from one $L1^{2-}$ ligand, one O_{phenol} atom, one N_{imine} atom and one $O_{carbonyl}$ atom from the other $L1^{2-}$ ligand, two O atoms from the D-pfc$^-$ anion, and one O_{DMF} atom. The Shape software analysis[51] showed that the coordination configurations of Dy1 and Dy3 in ***D*-2** are the triangular dodecahedron, with CShM values of 2.589 and 2.406, respectively (Table S4†), while Dy2 and Dy4 have the biaugmented trigonal prism J50 and biaugmented trigonal prism coordination configurations, with CShM values of 2.589 and 2.564, respectively (Table S4†). The crystal

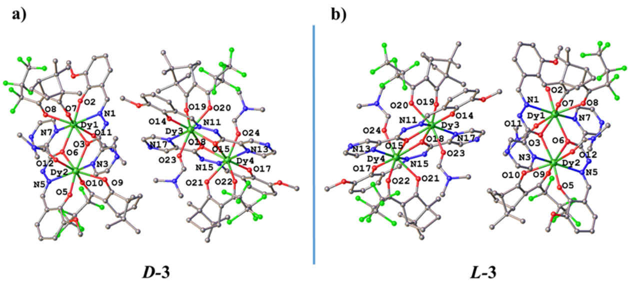

Fig. 3 Crystal structures of ***D*-3(a)** and ***L*-3(b)**; all H atoms are omitted for clarity.

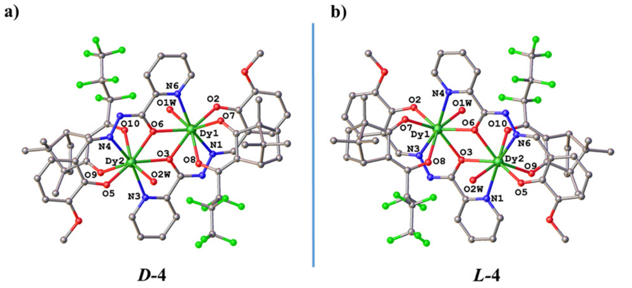

Fig. 4 Crystal structures of ***D*-4(a)** and ***L*-4(b)**; all H atoms and solvent molecules are omitted for clarity.

structure of ***L*-3** (Fig. 3b) is very similar to that of ***D*-3** (Fig. 3a), but ***L*-3** is mirror-symmetrical to ***D*-3** (Fig. 3).

Interestingly, ***D*-4** and ***L*-4** are crystallized in $P2_1$ again. As shown in Fig. 4a, the crystal structure of ***D*-4** is similar to that of ***D*-2** (Fig. 2a), except that the terminal ligand changes from D-tfc⁻ to D-pfc⁻. Two Dy^{3+} cations in ***D*-4** are chelated by two $L2^{2-}$ ligands of an approximate plane in opposite directions, and the D-pfc⁻ terminal ligands coordinated to different Dy^{3+} cations are located on the upper and lower sides of the approximately planar $[Dy_2(L2)_2]$, as are the water terminal ligands. The Dy1⋯Dy2 distance of 3.918 Å in ***D*-4** is slightly longer than the Dy⋯Dy distances of ***D*-1**, ***D*-2** and ***D*-3**. The Shape software analysis[51] showed that the coordination configurations of Dy1 and Dy2 in ***D*-4** are the triangular dodecahedron, with CShM values of 2.193 and 2.365, respectively (Table S5†). The crystal structure of ***L*-4** (Fig. 4b) is very similar to that of ***D*-4** (Fig. 4a), but ***L*-4** is mirror-symmetrical to ***D*-4** (Fig. 4).

Magnetic properties

Since the magnetic properties of enantiomers are very similar, we only need to measure the magnetic properties of their D-configuration isomers. As shown in Fig. 5, the $\chi_M T$ values of ***D*-1**, ***D*-2**, ***D*-3** and ***D*-4** at 300 K are 28.36, 28.35, 28.33 and 28.29 cm^3 $Kmol^{-1}$, respectively. All of them are very close to the calculated value of the two uncoupled Dy(III) ions (28.34 cm^3 $Kmol^{-1}$). As the temperature decreases, the $\chi_M T$ values of the four isomers all decrease slowly at low temperatures to reach a minimum value (26.66 cm^3 $Kmol^{-1}$ at 22 K for ***D*-1**, 26.70 cm^3 $Kmol^{-1}$ at 24 K for ***D*-2**, 26.99 cm^3 $Kmol^{-1}$ at 40 K for ***D*-3**, and 25.51 cm^3 $Kmol^{-1}$ at 26 K for ***D*-4**), and as the temperature continues to drop, their $\chi_M T$ values increase abruptly, reaching the maximum measured value at 2 K (34.40 cm^3 $Kmol^{-1}$ for ***D*-1**, 34.26 cm^3 $Kmol^{-1}$ for ***D*-2**, 40.09 cm^3 $Kmol^{-1}$ for ***D*-3**, and 35.99 cm^3 $Kmol^{-1}$ for ***D*-4**). This trend of $\chi_M T$–T change is the result of the synergistic effect of two factors, the depopulation of the M_j levels of the Dy^{3+} ion and the ferromagnetic interaction between the Dy^{3+} ions, in the Dy_2 complexes.[24,46,52] The magnetization of ***D*-1**, ***D*-2**, ***D*-3** and ***D*-4** as a function of the magnetic field was measured and shown as M–H/T curves (Fig. S1–S4†), and the M–H/T curves for each isomer do not coincide at different temperatures (2–6 K), indicating the presence of magnetic anisotropy in these isomers.

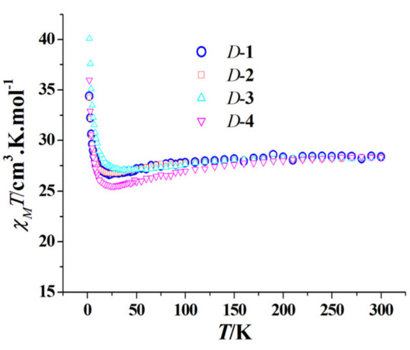

Fig. 5 Plots of $\chi_M T$ *versus* T of **D-1**, **D-2**, **D-3** and **D-4** (H_{dc} = 1000 Oe).

We then measured the ac magnetic susceptibility of ***D*-1**, ***D*-2**, ***D*-3** and ***D*-4** at a zero dc field in order to further explore their SMM properties. As shown in Fig. 6a, the χ''–T curves of ***D*-1** at 10–1399 Hz exhibit an obvious frequency dependence, with temperature peaks appearing from 401 Hz to 1399 Hz. The χ''–ν curves of ***D*-1** at 2.0–8.0 K also show clear peaks (Fig. 6b), and the ln τ *versus* 1/T plot was obtained from these frequency peaks corresponding to different temperatures (Fig. 6c), which presents a curve and could be fitted with the formula $\tau^{-1} = \tau_{QTM}{}^{-1} + CT^n + \tau_0{}^{-1}\exp(-U_{eff}/kT)$, giving τ_{QTM} = 0.00279(0.00013) s, n = 4.14(0.38), C = 0.9596(0.0915) s^{-1} $K^{-4.14}$ U_{eff}/k = 47.6(1.4) K and τ_0 = 2.1(0.2) × 10^{-11} s. Either the τ_0 value of 2.1 × 10^{-11} s (10^{-6} s–10^{-11} s) or the n value of 4.14 ($2 < n < 9$) is within the normal range. The U_{eff}/k value of ***D*-1** (47.6 K) is a little larger than that of $[Dy_2(L2)_2(acac)_2(EtOH)_2]$ (45 K at 0 Oe).[50] The semicircular Cole–Cole plots suggest that ***D*-1** exhibits a single magnetic relaxation process, which could

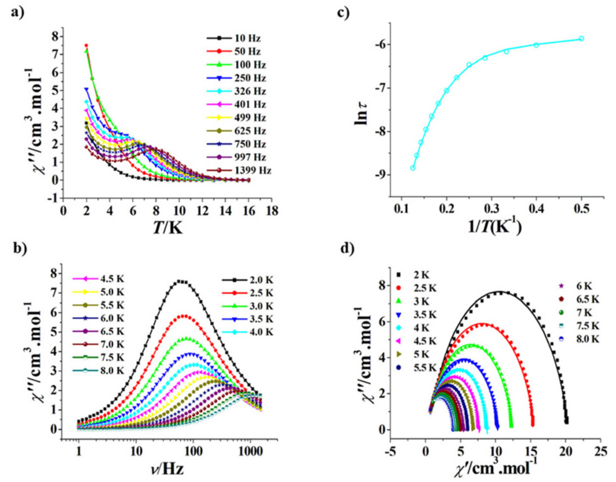

Fig. 6 Plots of χ'' *versus* T for **D-1** (H_{dc} = 0 Oe) (a). Frequency dependence of χ'' for **D-1** at a zero dc field (b). Plot of ln (τ) *versus* 1/T for **D-1** (H_{dc} = 0 Oe); the solid line represents the best fitting with quantum tunnelling plus Orbach plus Raman (c). Cole–Cole plots measured from 2.0 to 8.0 K for **D-1** (H_{dc} = 0 Oe); the solid lines represent the best fitting with the generalized Debye model (d).

be fitted by a generalized Debye model (Fig. 6d),[53,54] giving the α value in the range of 0.079–0.149. These relatively small α-values mean that ***D*-1** has a relatively narrow relaxation time distribution. When the temperature drops to 1.9 K, no hysteresis loop of ***D*-1** could be observed (Fig. S5†).

We also investigated the effect of the dc magnetic field on the magnetic relaxation of ***D*-1**. At 1500 Oe, a commonly used magnetic field, the peak shape of the χ''–T curve of ***D*-1** is more obvious, and the peak range (5–1399 Hz) is larger than that of the zero dc magnetic field (401 Hz–1399 Hz) (Fig. S6a†). These changes caused by the 1500 Oe field suggest that it can inhibit the quantum tunnelling effect. The temperature range for peaking in the χ''–ν curve at 1500 Oe (3.5 K–8.5 K) is also wider than that at 0 Oe (2.0 K–8.0 K) (Fig. S6b†). The ln τ *versus* 1/T plot based on the χ''–ν curves at 1500 Oe of ***D*-1** could be fitted by the formula $\tau^{-1} = CT^n + \tau_0{}^{-1}\exp(-U_{\text{eff}}/kT)$ (Fig. S6c†), giving n = 5.91(0.43), C = 0.0147(0.0081) s^{-1} K$^{-5.91}$, U_{eff}/k = 50.5(5.0) K and τ_0 = 1.5(0.2) × 10^{-11} s. As with other zero-field SMMs,[15,27] the U_{eff}/k value of ***D*-1** at 1500 Oe (50.5 K) is larger than at 0 Oe (47.6 K), and the τ_0 value of ***D*-1** at 1500 Oe (1.5 × 10^{-11} s) is smaller than that at 0 Oe (2.1 × 10^{-11} s).

At 0 Oe, the χ''–T curves of ***D*-2** at 10–1399 Hz show a more pronounced frequency dependence than ***D*-1**, with the peaking frequency starting at 25 Hz (Fig. 7a). The temperature region (2.0–10.5 K) with a peak in the χ''–ν curve at 0 Oe (Fig. 7b) is also wider than that of ***D*-1** (2.0–8.0 K). The ln τ *versus* 1/T plot of ***D*-2** based on the χ''–ν curve is also a curve (Fig. 7c), which could likewise be fitted by $\tau^{-1} = \tau_{\text{QTM}}{}^{-1} + CT^n + \tau_0{}^{-1}\exp(-U_{\text{eff}}/kT)$ to give τ_{QTM} = 0.00369(0.00218) s, n = 5.52(0.19), C = 0.0285 (0.0095) s^{-1} K$^{-5.25}$, U_{eff}/k = 152.2(7.8) K and τ_0 = 1.5(0.2) × 10^{-11} s. The τ_0 value of ***D*-2** (1.5 × 10^{-11} s) is comparable to that of ***D*-1** (2.1 × 10^{-11} s), but the U_{eff}/k value of ***D*-2** (152.2 K) is obviously larger than that of ***D*-1** (47.6 K). The Cole–Cole plots of ***D*-2** are semicircular too, indicating a single magnetic relaxation process, and these χ''–χ' curves could also be fitted by a generalized Debye model (Fig. 7d),[53,54] giving the α value of 0.008–0.130. These α values are relatively small, meaning that ***D*-2** also has a relatively narrow relaxation time distribution. Similar to ***D*-1**, the hysteresis loop couldn't be observed at 1.9 K for ***D*-2** (Fig. S7†).

Similar to ***D*-1**, the peak shape of the χ''–T curve of ***D*-2** at 1500 Oe is more obvious than at 0 Oe, and the peaking range (10–1399 Hz) is somewhat larger than that at 0 Oe (25 Hz–1399 Hz) (Fig. S8a†). However, the temperature range for peaking in the χ''–ν curve at 1500 Oe (4.0 K–10.5 K) is narrower than that at 0 Oe (2.0 K–10.5 K) (Fig. S8b†). The ln τ *versus* 1/T plot based on the χ''–ν curves at 1500 Oe could also be fitted by the formula $\tau^{-1} = CT^n + \tau_0{}^{-1}\exp(-U_{\text{eff}}/kT)$ (Fig. S8c†), giving n = 6.47(0.08), C = 0.00222(0.00034) s^{-1} K$^{-6.47}$, U_{eff}/k = 160.6(4.8) K and τ_0 = 1.1(0.1) × 10^{-11} s. Similar to ***D*-1**, the U_{eff}/k value of ***D*-2** at 1500 Oe (160.6 K) is larger than that at 0 Oe (152.2 K), and the τ_0 value of ***D*-2** at 1500 Oe (1.1 × 10^{-11} s) is smaller than that at 0 Oe (1.5 × 10^{-11} s).

At 0 Oe, the frequency dependence of the χ''–T curve of ***D*-3** is even more pronounced, with a temperature peak beginning at 5 Hz (Fig. 8a). The χ''–ν curve of ***D*-3** at 0 Oe still has a frequency peak at 17 K, but it no longer occurs below 5 K (Fig. 8b). The ln τ *versus* 1/T plot of ***D*-3** according to the frequency peak values at different temperatures (5–17 K) is a curve again (Fig. 8c), which could be fitted by $\tau^{-1} = \tau_{\text{QTM}}{}^{-1} + CT^n + \tau_0{}^{-1}\exp(-U_{\text{eff}}/kT)$ too, giving τ_{QTM} = 0.1624(0.042) s, n = 5.33(0.21), C = 0.00132(0.00062) s^{-1} K$^{-5.33}$, U_{eff}/k = 173.8(7.4) K and τ_0 = 1.9(0.2) × 10^{-8} s. The U_{eff}/k value of ***D*-3** (173.8 K) is larger than that of ***D*-2** (152.2 K). The semicircle of the Cole–

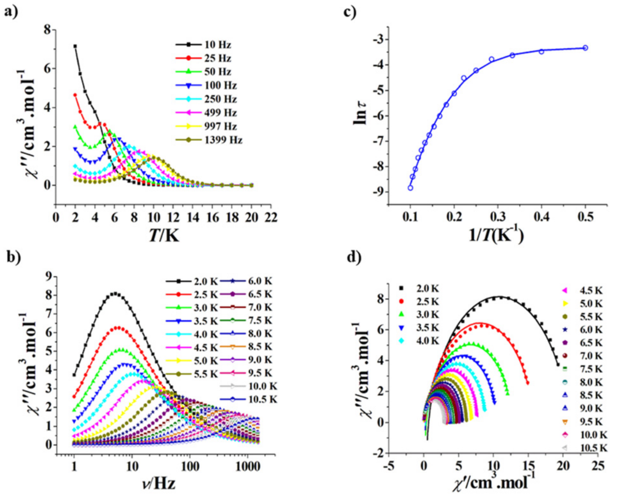

Fig. 7 Plots of χ'' *versus* T for ***D*-2** (H_{dc} = 0 Oe) (a). Frequency dependence of χ'' for ***D*-2** at a zero dc field (b). Plot of ln (τ) *versus* 1/T for ***D*-2** (H_{dc} = 0 Oe); the solid line represents the best fitting with quantum tunnelling plus Orbach plus Raman (c). Cole–Cole plots measured from 2.0 to 10.5 K for ***D*-2** (H_{dc} = 0 Oe); the solid lines represent the best fitting with the generalized Debye model (d).

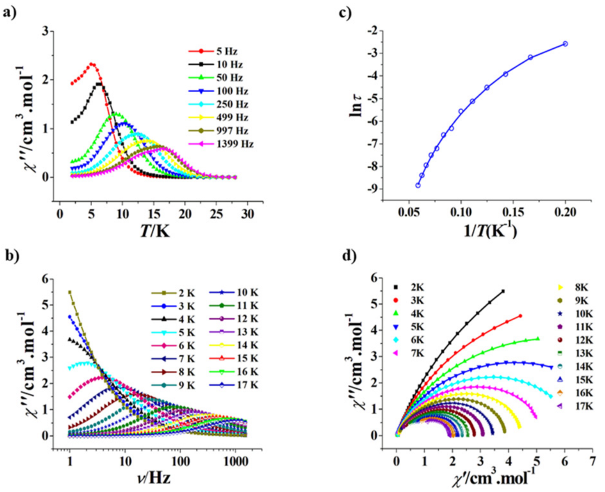

Fig. 8 Plots of χ'' *versus* T for ***D*-3** (H_{dc} = 0 Oe) (a). Frequency dependence of χ'' for ***D*-3** at a zero dc field (b). Plot of ln (τ) *versus* 1/T for ***D*-3** (H_{dc} = 0 Oe); the solid line represents the best fitting with quantum tunnelling plus Orbach plus Raman (c). Cole–Cole plots measured from 2.0 to 17 K for ***D*-3** (H_{dc} = 0 Oe); the solid lines represent the best fitting with the sum of two modified Debye functions (d).

Cole diagram of ***D*-3** is not very obvious (Fig. 8d), and these χ''–χ' curves are not as well fit with the generalized Debye model[53,54] as they are with the sum of two modified Debye functions,[55–57] suggesting that ***D*-3** has the characteristic of double magnetic relaxation. This may be related to the presence of two crystallographically independent molecules in the crystal structure of ***D*-3**. The α_1 values were fitted to be 0.006–0.223 and the α_2 values to be 0.011–0.222. Furthermore, the hysteresis loop of ***D*-3** could not be observed at 1.9 K too (Fig. S9†).

The peak shape of the χ''–T curve of ***D*-3** at 1500 Oe is more obvious than at 0 Oe, but the peaking range (5–1399 Hz) is the same as that at 0 Oe (5 Hz–1399 Hz) (Fig. S10a†). Moreover, the temperature range for showing a peak in the χ''–ν curve at 1500 Oe (5 K–17 K) is the same as that at 0 Oe (5 K–17 K) (Fig. S10b†). The $\ln\tau$ *versus* $1/T$ plot based on these χ''–ν curves at 1500 Oe could also be fitted by the formula $\tau^{-1} = CT^n + \tau_0^{-1}\exp(-U_{\mathrm{eff}}/kT)$ (Fig. S10c†), giving n = 4.53(0.09), C = 0.00943(0.00168) $\mathrm{s^{-1}\ K^{-4.53}}$, U_{eff}/k = 179.0(5.8) K and τ_0 = 7.8 (0.2) × 10^{-9} s. Similar to ***D*-1** and ***D*-2**, the U_{eff}/k value of ***D*-3** at 1500 Oe (179.0 K) is larger than that at 0 Oe (173.8 K), and the τ_0 value of ***D*-3** at 1500 Oe (7.8 × 10^{-9} s) is smaller than that at 0 Oe (1.9 × 10^{-8} s).

The ac magnetic susceptibility of ***D*-4** at 0 Oe is similar to those of ***D*-1** and ***D*-2**. As shown in Fig. 9a, the frequency dependence can be observed in the χ''–T curves of ***D*-4** at 5–1399 Hz, where they show peaks in the range of 250 Hz–1399 Hz. In the χ''–ν curves of ***D*-4** at 0 Oe, the peaks can be seen in the range of 2–9.5 K (Fig. 9b), and the $\ln\tau$ *versus* $1/T$ plot could be derived from these frequency peaks at different temperatures (Fig. 9c), which could also be fitted with the formula $\tau^{-1} = \tau_{\mathrm{QTM}}^{-1} + CT^n + \tau_0^{-1}\exp(-U_{\mathrm{eff}}/kT)$, yielding τ_{QTM} = 0.00521(0.00029) s, n = 3.81(0.19), C = 0.83093(0.07773) $\mathrm{s^{-1}\ K^{-3.81}}$, U_{eff}/k = 116.2(6.7) K and τ_0 = 1.4(0.1) × 10^{-9} s. The U_{eff}/k value of ***D*-4** (116.2 K) is larger than that of ***D*-1** (47.6 K), but smaller than those of ***D*-2** (152.2 K) and ***D*-3** (173.8 K). Like ***D*-1** and ***D*-2**, the Cole–Cole diagram of ***D*-4** also shows the semicircular shape (Fig. 9d), suggesting that only a single magnetic relaxation process exists in ***D*-4**. These χ''–χ' curves could be fitted by a generalized Debye model too (Fig. 9d),[53,54] yielding a relatively small α value of 0.041–0.157, implying that ***D*-4** exhibits a relatively narrow relaxation time distribution. Similar to ***D*-1** and ***D*-2**, at 1.9 K no hysteresis loop could be observed for ***D*-4** (Fig. S11†).

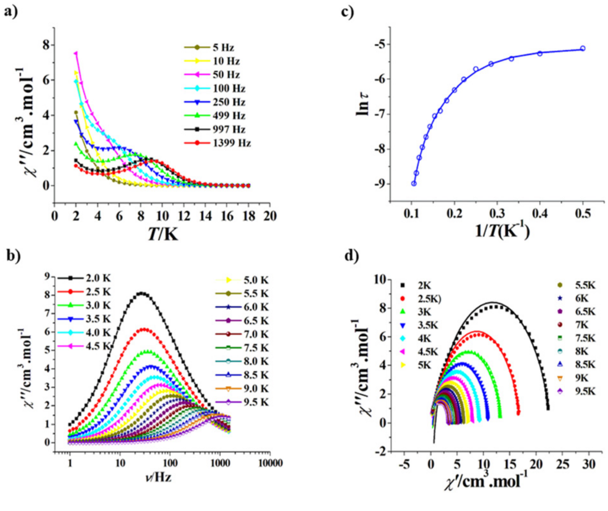

Fig. 9 Plots of χ'' *versus* T for ***D*-4** (H_{dc} = 0 Oe) (a). Frequency dependence of χ'' for ***D*-4** at a zero dc field (b). Plot of ln (τ) *versus* $1/T$ for ***D*-4** (H_{dc} = 0 Oe); the solid line represents the best fitting with quantum tunnelling plus Orbach plus Raman (c). Cole–Cole plots measured from 2.0 to 9.5 K for ***D*-4** (H_{dc} = 0 Oe); the solid lines represent the best fitting with the generalized Debye model (d).

The peak shape of the χ''–T curve of ***D*-4** at 1500 Oe is more obvious than at 0 Oe, and the peaking range (5–1399 Hz) is obviously larger than that at 0 Oe (250 Hz–1399 Hz) (Fig. S12a†). However, the temperature range for showing a peak in the χ''–ν curve at 1500 Oe (3.0 K–9.5 K) is a little narrower than that at 0 Oe (2.0 K–9.5 K) (Fig. S12b†). The $\ln\tau$ *versus* $1/T$ plot based on the χ''–ν curves at 1500 Oe could also be fitted by the formula $\tau^{-1} = CT^n + \tau_0^{-1}\exp(-U_{\mathrm{eff}}/kT)$ (Fig. S12c†), giving n = 4.94(0.15), C = 0.06787 (0.01576) $\mathrm{s^{-1}\ K^{-4.94}}$, U_{eff}/k = 119.2(6.8) K and τ_0 = 1.1(0.1) × 10^{-9} s. Similar to ***D*-1**, ***D*-2** and ***D*-3**, the U_{eff}/k value of ***D*-4** at 1500 Oe (119.2 K) is larger than that at 0 Oe (116.2 K), and the τ_0 value of ***D*-4** at 1500 Oe (1.1 × 10^{-9} s) is smaller than that at 0 Oe (1.4 × 10^{-11} s).

Theoretical calculations

Ab initio calculations[58,59] for ***D*-1**, ***D*-2**, ***D*-3** and ***D*-4** were performed with the MOLCAS 8.1 program[60] in order to better understand their magnetic properties. Because there is a small geometric difference between the two Dy(III) centers in each molecule, we calculate the two magnetic centers separately. The calculated fragment is based on the crystal structure, but the other Dy(III) ion is replaced by a diamagnetic Lu(III) ion. The calculated results are listed in Tables S6–S9.† ***D*-1**, ***D*-2**, ***D*-3** and ***D*-4** have similar low-lying Kramers doublets (KDs), whose ground states are mainly composed of $m_J = \pm 15/2$. The g values for the ground state are as follows: g_x = 0.019, g_y = 0.024, and g_z = 19.541 of Dy1 and g_x = 0.023, g_y = 0.029, and g_z = 19.543 of Dy2 for ***D*-1** (Table S6†); g_x = 0.024, g_y = 0.037, and g_z = 19.504 of Dy1 and g_x = 0.014, g_y = 0.020, and g_z = 19.460 of Dy2 for ***D*-2** (Table S7†); g_x = 0.007, g_y = 0.010, and g_z = 19.679 of Dy1, g_x = 0.003, g_y = 0.005, and g_z = 19.641 of Dy2, g_x = 0.006, g_y = 0.009, and g_z = 19.691 of Dy3, and g_x = 0.006, g_y = 0.012, and g_z = 19.485 of Dy4 for ***D*-3** (Table S8†); and g_x = 0.006, g_y = 0.029, and g_z = 19.454 of Dy1 and g_x = 0.001, g_y = 0.016, and g_z = 19.532 of Dy2 for ***D*-4** (Table S9†). All these g values are very similar to those of the Ising limit states for the Dy(III) ion (supposed $S = \pm 1/2$), suggesting that their magnetic interaction belongs to the Ising type.

Based on the calculated mean values of the magnetic moment matrix elements between the electronic states, it is predicted that the magnetization reversal by thermally assisted quantum tunnelling of magnetization (TA-QTM) will occur in the first excited states (Tables S10–S13†). The deduced energy barriers are as follows: 183.6 K of Dy1 and 192.2 K of Dy2 for ***D*-1** (Table S10†); 180.3 K of Dy1 and 193.0 K of Dy2 for ***D*-2** (Table S11†); 294.5 K of Dy1, 294.5 K of Dy2, 304.5 K of Dy3 and 252.8 K of Dy4 for ***D*-3** (Table S12†); 161.0 K of Dy1 and 174.5 K of Dy2 for ***D*-4** (Table S13†). The theoretical energy barriers of ***D*-1**, ***D*-2**, ***D*-3** and ***D*-4** are larger than the corresponding experimental U_{eff}/k values: 47.6 K for ***D*-1**, 152.2 K for ***D*-2**, 173.8 K for ***D*-3**; and 116.2 K for ***D*-4**, which can be attributed to the existence of Raman magnetic relaxation and QTM.[52] It is worth mentioning that the experimental U_{eff}/k value of ***D*-3**, which has the highest theoretical value, is also the highest.

The Dy(III)–Dy(III) magnetic interaction within each molecule of ***D*-1**, ***D*-2**, ***D*-3** and ***D*-4** was analysed using the POLY_ANISO program.[58,59] As usual, $J_{\mathrm{total}} = J_{\mathrm{dip}} + J_{\mathrm{exch}}$, in which J_{total} is the total coupling interaction and J_{exch} and J_{dip} represent the exchange interaction and the dipole–dipole interaction, respectively. The J_{total} values were obtained after using the Lines model[61] to fit χT *versus* T plots of ***D*-1**, ***D*-2**, ***D*-3** and ***D*-4** (Fig. S13†). As shown in Table 1, the J_{dip} values of ***D*-3** (5.06 and 4.75 cm^{-1}) are larger than those of ***D*-1**, ***D*-2** and ***D*-4** (4.11 cm^{-1}), and only the J_{exch} values of ***D*-3** are positive (0.50 and 1.00 cm^{-1}). As a result, the J_{total} value of ***D*-3** is obviously larger than those of the other three isomers (***D*-1**, ***D*-2** and ***D*-4**). As mentioned above, the energy barrier value of ***D*-3** is also larger than those of the other three isomers (***D*-1**, ***D*-2** and ***D*-4**), which suggests that a larger J_{total} value is beneficial for increasing the energy barrier value of this type of Dy_2 SMMs. By the way, all four isomers have a positive J_{total} value (Table 1), indicating the Dy(III)–Dy(III) ferromagnetic interaction. Therefore, the main magnetic axes on the Dy(III) ions of ***D*-1**, ***D*-2**, ***D*-3** and ***D*-4** are arranged approximately in parallel (Fig. S14–S17†).

Circular dichroism (CD) spectra and magnetic circular dichroism (MCD) properties

The circular dichroism (CD) spectra of these four pairs of enantiomers in DMF solution were recorded at room temperature, and they show chiral optical activities and chiral enantiomer nature (Fig. 10 and 11). At 0 T, the CD spectra of ***D*-1/*L*-1**, ***D*-2/*L*-2**, ***D*-3/*L*-3** and ***D*-4/*L*-4** in DMF solution display mirror symmetry in the range of 280–500 nm, with a strong peak at 307 nm and two weak peaks at 399 nm and 457 nm for ***D*-1/*L*-1**; a strong peak at 309 nm and a weak peak at 399 nm for ***D*-2/*L*-2**; a strong peak at 310 nm and a weak peak at 397 nm for ***D*-3/*L*-3**; a strong peak at 311 nm and a weak peak at 408 nm for ***D*-4/*L*-4**. Referring to their UV spectra (Fig. 10b, d and 11b, d), the Cotton effect at 307 nm-311 nm is caused by the π–π^* transitions of the homochiral β-diketone ligands (D-tfc$^-$/L-tfc$^-$ and D-pfc$^-$/L-pfc$^-$), while the Cotton effect at 397 nm–408 nm (and an additional 457 nm for ***D*-1/*L*-1**) should be ascribed to the π–π^* transition and n–π^* transition of the chromatophores (–HC=NN) of the hydrazone Schiff base ligands ($\mathrm{L1}^{-2}$ and $\mathrm{L2}^{-2}$).

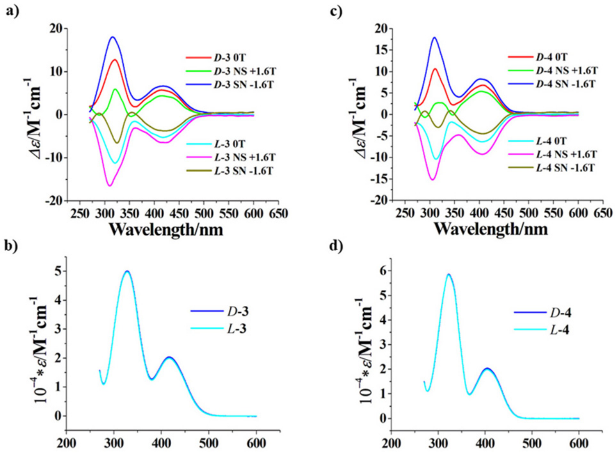

Fig. 10 CD spectra (H = 0 T) and MCD spectra (H = ±1.6 T, 5 mm optical path) (a) and UV spectra (b) of ***D*-1/*L*-1** in a DMF solution (c = 0.2 g L^{-1}) at room temperature; CD spectra (H = 0 T) and MCD spectra (H = ±1.6 T, 5 mm optical path) (c) and UV spectra (d) of ***D*-2/*L*-2** in a DMF solution (c = 0.2 g L^{-1}) at room temperature.

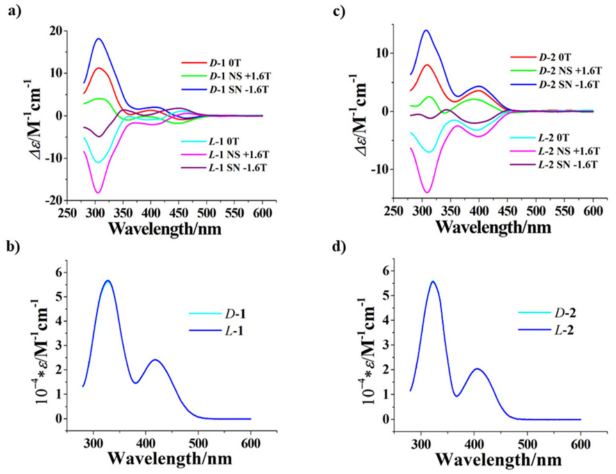

Fig. 11 CD spectra (H = 0 T) and MCD spectra (H = ±1.6 T, 5 mm optical path) (a) and UV spectra (b) of ***D*-3/*L*-3** in a DMF solution (c = 0.2 g L^{-1}) at room temperature; CD spectra (H = 0 T) and MCD spectra (H = ±1.6 T, 5 mm optical path) (c) and UV spectra (d) of ***D*-4/*L*-4** in a DMF solution (c = 0.2 g L^{-1}) at room temperature.

Table 1 The magnetic interactions (cm^{-1}) obtained using the Lines model

			***D*-3**		
	***D*-1**	***D*-2**	Dy1–Dy2	Dy3–Dy4	***D*-4**
J_{dip}	4.11	4.11	5.06	4.75	4.11
J_{exch}	−1.00	−0.75	0.50	1.00	−1.00
J_{total}	3.11	3.36	5.56	5.75	3.11

The MCD spectra of these four pairs of enantiomers in DMF solution were then recorded at ±1.6 T (Fig. 10 and 11), for evaluating their magneto-optical Faraday effects. It is positive (+1.6 T) when the positive direction (NS) of the magnetic field is parallel to the polarized light, and conversely, negative (−1.6 T) when the opposite direction (SN) of the magnetic field is parallel to the polarized light. As can be seen from Fig. 10

and 11, the SN (−1.6 T) CD curve for the D-isomer is roughly symmetrical with the NS (+1.6 T) CD curve for the L-isomer. Similarly, the NS (+1.6 T) CD curve for the D-isomer is roughly symmetrical with the SN (−1.6 T) CD curve for the L-isomer. According to MCD = [CD(+1.0 T) − CD(−1.0 T)]/2,[24,25] the pure MCD spectra of ***D*-1**/***L*-1**, ***D*-2**/***L*-2**, ***D*-3**/***L*-3** and ***D*-4**/***L*-4** were obtained, which exhibit a strong peak at 306 nm/304 nm for ***D*-1**/***L*-1** (Fig. S18†), at 305 nm/308 nm for ***D*-2**/***L*-2** (Fig. S19†), at 310 nm/306 nm for ***D*-3**/***L*-3** (Fig. S20†), and at 308 nm/301 nm for ***D*-4**/***L*-4** (Fig. S21†), which are attributed to the π–π* transitions of the homochiral β-diketone ligands (D-tfc$^-$/L-tfc$^-$, D-pfc$^-$/L-pfc$^-$).

The anisotropy factor g_{MCD} of the MCD spectra in the π–π* and n–π* transition regions could also be calculated,[62] and the absolute value of its extreme value can reflect the strength of the magneto-optical Faraday effect. As shown in Fig. S22–S25,† the wavelength-dependent g_{MCD} curves of the D-isomer and the L-isomer display mirror-symmetry approximately for all four pairs of enantiomers. The $g_{\max(\mathrm{MCD})}$ values are −0.78 T^{-1} and 0.82 T^{-1} for ***D*-1** and ***L*-1**, respectively (Fig. S22†); −0.34 T^{-1} and 0.36 T^{-1} for ***D*-2** and ***L*-2**, respectively (Fig. S23†); −0.38 T^{-1} and 0.42 T^{-1} for ***D*-3** and ***L*-3**, respectively (Fig. S24†); −0.34 T^{-1} and 0.42 T^{-1} for ***D*-4** and ***L*-4**, respectively (Fig. S25†). The $|g_{\max(\mathrm{MCD})}|$ values of these four pairs of enantiomers (0.34–0.82 T^{-1}) are the largest among the complexes,[27] which are clearly larger than those of 4f mononuclear complexes (≤0.24 T^{-1})[44] and most of the 3d–4f complexes,[25,26] but smaller than those of $[\mathrm{Dy_2(L\text{-}tfc)_4(chp)_2(MeOH)_2}]$/$[\mathrm{Dy_2(D\text{-}tfc)_4(chp)_2(MeOH)_2}]$ (Hchp = 6-chloro-2-hydroxypyridine) (1.27/1.72 T^{-1}).[24] Since g_{MChD} is proportional to g_{MCD},[63] it is expected that these enantiomers will also have relatively larger g_{MChD} values.

SHG and THG nonlinear optical properties

Since the second-harmonic generation (SHG) and the third harmonic generation (THG) responses of the D- and L-chiral isomers are very similar, we only need to measure the nonlinear optical properties of the D-chiral isomers in the solid state. As shown in Fig. S26,† the SHG intensities of ***D*-1**, ***D*-2**, ***D*-3** and ***D*-4** at room temperature are lower compared to the reference KDP, and the order of SHG intensities is ***D*-1** > ***D*-2** > ***D*-3** > ***D*-4**. The $\chi_{\mathrm{R}}^{(2)}$ value of KDP is known to be 0.39 pm V^{-1},[64] and the $\chi_{\mathrm{S}}^{(2)}$ values of these chiral isomers (***D*-1**, ***D*-2**, ***D*-3** and ***D*-4**) could be thus calculated,[16] as shown in Table 2.

However, the THG intensities of ***D*-1**, ***D*-2**, ***D*-3** and ***D*-4** are surprisingly strong compared to the reference α-SiO$_2$ (Fig. 12), and the order of THG intensities is ***D*-1** (661.8 × α-SiO$_2$) > ***D*-3** (133.2 × α-SiO$_2$) > ***D*-2** (73.0 × α-SiO$_2$) > ***D*-4** (18.5 × α-SiO$_2$). Notably, examples of chiral isomers with THG being more prominent than SHG are uncommon, and only a few have been reported.[31] The $\chi_{\mathrm{S}}^{(3)}$ values of these chiral isomers could be calculated[16] based on the $\chi_{\mathrm{R}}^{(3)}$ value of the reference α-SiO$_2$ of 214 pm^{2}V^{-2}.[65] As shown in Table 2, ***D*-1** has the strongest $\chi_{\mathrm{S}}^{(3)}$ value (5505 pm^2 V^{-2}), which is 25.7 times that of the reference α-SiO$_2$ (214 pm^2 V^{-2}), and much larger than those of Dy$^{\mathrm{III}}$-β-diketonate with homochiral N-donors(≤1267 pm^2 V^{-2}).[16] Notably, to the best of our knowledge, ***D*-1** displays the strongest THG response (661.8 × α-SiO$_2$) among the lanthanide(III) complexes, showing the potential for application in nonlinear optical materials or devices. The significant THG in ***D*-1**, ***D*-2**, ***D*-3** and ***D*-4** can be attributed to three factors: (a) the deprotonated hydrazone Schiff base ligands L1^{-2} and L2^{-2} are large π-electron conjugated ligands; (b) the formation of coordination bonds of Dy–N and Dy–O, leading to the delocalization of the π electron cloud;[66] and (c) owing to the presence of the $-\mathrm{CF_3}$ group in D-tfc$^-$/L-tfc$^-$ and the $-\mathrm{C_3F_7}$ group in D-pfc$^-$/L-pfc$^-$ ligands, they become an electronic 'pull–push' system, which makes the molecule highly polarizable and conducive to the occurrence of polarization-dependent THG signals.[67]

Table 2 $\chi_{\mathrm{S}}^{(2)}$ and $\chi_{\mathrm{S}}^{(3)}$ values of ***D*-1**, ***D*-2**, **D-3** and **D-4**

	***D*-1**	***D*-2**	***D*-3**	***D*-4**
$\chi_{\mathrm{S}}^{(2)}$/pm V^{-1}	0.104	0.045	0.021	0.015
$\chi_{\mathrm{S}}^{(3)}$/pm^2 V^{-2}	5505	1828	2469	921

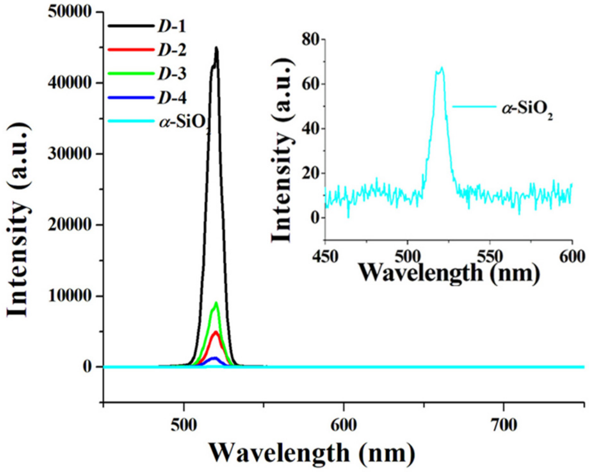

Fig. 12 THG spectra of crystalline samples of ***D*-1**, ***D*-2**, ***D*-3**, ***D*-4** and α-SiO$_2$ (illustration) under excitation at λ = 1550 nm (T_{int} = 0.5 s).

The structural difference between ***D*-1** and ***D*-2** as well as between ***D*-3** and ***D*-4** is mainly that ***D*-1** and ***D*-3** contain a pyrazine ring in the hydrazone Schiff base ligand L1^{-2}, while ***D*-2** and ***D*-4** contain a pyridine ring in the hydrazone Schiff base ligand L2^{-2}. From Table 2, it can be seen that the $\chi_{\mathrm{S}}^{(2)}$ value and the $\chi_{\mathrm{S}}^{(3)}$ value of ***D*-1** (or ***D*-3**) are significantly larger than those of ***D*-2** (or ***D*-4**), indicating that the pyrazine ring of the hydrazone Schiff base ligand in this Dy$_2$ molecular system is more conducive to obtaining better second- or third-order nonlinear optical properties than the pyridine ring.

The structural difference between ***D*-1** and ***D*-3** as well as between ***D*-2** and ***D*-4** is mainly that ***D*-1** and ***D*-2** contain D-tfc$^-$ with the trifluoromethyl group, while ***D*-3** and ***D*-4** contain D-pfc$^-$ with the heptafluoropropyl group. From Table 2, it can be seen that the $\chi_{\mathrm{S}}^{(2)}$ value and the $\chi_{\mathrm{S}}^{(3)}$ value of ***D*-1** (or ***D*-2**) are obviously larger than those of ***D*-3** (or ***D*-4**), indicating that the trifluoromethyl group of the β-diketone ligand in this Dy$_2$

molecular system is more conducive to obtaining better second- or third-order nonlinear optical properties than the heptafluoropropyl group.

Conclusion

In summary, four pairs of homochiral dysprosium(III) dinuclear complexes were directionally constructed using homochiral β-diketone terminal ligands and hydrazone Schiff base bridging ligands, which show good SMM behaviors at 0 Oe and strong magneto-optical Faraday effects at room temperature. Surprisingly, these four pairs of enantiomers display strong THG, and among them, ***D*-1** exhibits the strongest THG response (661.8 × α-SiO_2) in the lanthanide(III) complexes. Obviously, the crystal structures, the magnetic behaviors, the magneto-optical Faraday effects and the nonlinear optical properties of such homochiral Dy_2 complexes can be affected by the heterocyclic groups (pyrazine *vs.* pyridine) on the hydrazone Schiff base bridging ligands and the length of the fluorocarbon chain on the homochiral β-diketone ligands. This work demonstrates that the precise construction of homochiral Dy_2 SMMs is feasible, and the structure and performance of such multifunctional SMMs can be modulated by the functional groups on the ligands.

Conflicts of interest

There are no conflicts to declare.

Acknowledgements

This research was generously funded by the National Natural Science Foundation of China (Grant Numbers 22271289, 21871274 and 22131003).

References

1 J. Long, M. S. Ivanov, V. A. Khomchenko, E. Mamontova, J. M. Thibaud, J. Rouquette, M. Beaudhuin, D. Granier, R. A. S. Ferreira, L. D. Carlos, B. Donnadieu, M. S. C. Henriques, J. A. Paixao, Y. Guari and J. Larionova, Room temperature magnetoelectric coupling in a molecular ferroelectric ytterbium(III) complex, *Science*, 2020, **367**, 671.

2 M. Atzori, K. Dhbaibi, H. Douib, M. Grasser, V. Dorcet, I. Breslavetz, K. Paillot, O. Cador, G. L. J. A. Rikken, B. Le Guennic, J. Crassous, F. Pointillart and C. Train, Helicene-Based Ligands Enable Strong Magneto-Chiral Dichroism in a Chiral Ytterbium Complex, *J. Am. Chem. Soc.*, 2021, **143**, 2671.

3 Z. Zhu, C. Zhao, T. Feng, X. Liu, X. Ying, X.-L. Li, Y.-Q. Zhang and J. Tang, Air-Stable Chiral Single-Molecule Magnets with Record Anisotropy Barrier Exceeding 1800 K, *J. Am. Chem. Soc.*, 2021, **143**, 10077.

4 K. Dhbaibi, M. Grasser, H. Douib, V. Dorcet, O. Cador, N. Vanthuyne, F. Riobé, O. Maury, S. Guy, A. Bensalah-Ledoux, B. Baguenard, G. L. J. A. Rikken, C. Train, B. Le Guennic, M. Atzori, F. Pointillart and J. Crassous, Multifunctional Helicene-Based Ytterbium Coordination Polymer Displaying Circularly Polarized Luminescence, Slow Magnetic Relaxation and Room Temperature Magneto-Chiral Dichroism, *Angew. Chem., Int. Ed.*, 2023, **62**, e202215558.

5 B.-F. Long, S. Yu, Z.-H. Zhu, Y.-L. Li, F.-P. Liang and H.-H. Zou, Coordination site manipulation of the annular growth mechanism to assemble chiral lanthanide clusters with different shapes and magnetic properties, *Inorg. Chem. Front.*, 2022, **9**, 5950.

6 C. Zhao, Z. Zhu, X.-L. Li and J. Tang, Air-stable chiral mono- and dinuclear dysprosium single-molecule magnets: steric hindrance of hexaazamacrocycles, *Inorg. Chem. Front.*, 2022, **9**, 4049.

7 C.-M. Liu, D.-Q. Zhang, X. Hao and D.-B. Zhu, Assembly of chiral 3d-4f wheel-like cluster complexes with achiral ligands: single-molecule magnetic behavior and magnetocaloric effect, *Inorg. Chem. Front.*, 2020, **7**, 3340.

8 J. Liu, X.-P. Zhang, T. Wu, B.-B. Ma, T.-W. Wang, C.-H. Li, Y.-Z. Li and X.-Z. You, Solvent-Induced Single-Crystal-to-Single-Crystal Transformation in Multifunctional Chiral Dysprosium(III) Compounds, *Inorg. Chem.*, 2012, **51**, 8649.

9 X.-L. Li, C.-L. Chen, Y.-L. Gao, C.-M. Liu, X.-L. Feng, Y.-H. Gui and S.-M. Fang, Modulation of Homochiral DyIII Complexes: Single-Molecule Magnets with Ferroelectric Properties, *Chem. – Eur. J.*, 2012, **18**, 14632.

10 X.-L. Li, M. Hu, Z. Yin, C. Zhu, C.-M. Liu, H.-P. Xiao and S. Fang, Enhanced single-ion magnetic and ferroelectric properties of mononuclear Dy(III) enantiomeric pairs through the coordination role of chiral ligands, *Chem. Commun.*, 2017, **53**, 3998.

11 P.-H. Guo, J.-L. Liu, J.-H. Jia, J. Wang, F.-S. Guo, Y.-C. Chen, W.-Q. Lin, J.-D. Leng, D.-H. Bao, X.-D. Zhang, J.-H. Luo and M.-L. Tong, Multifunctional $Dy^{III}{}_4$ Cluster Exhibiting White-Emitting, Ferroelectric and Single-Molecule Magnet Behavior, *Chem. – Eur. J.*, 2013, **19**, 8769.

12 R. Akiyoshi, H. Zenno, Y. Sekine, M. Nakaya, M. Akita, D. Kosumi, L. F. Lindoy and S. Hayami, A Ferroelectric Metallomesogen Exhibiting Field-Induced Slow Magnetic Relaxation, *Chem. – Eur. J.*, 2022, **28**, e202103367.

13 C.-M. Liu, D.-Q. Zhang, R.-G. Xiong, X. Hao and D.-B. Zhu, A homochiral Zn-Dy heterometallic left-handed helical chain complex without chiral ligands: anion-induced assembly and multifunctional integration, *Chem. Commun.*, 2018, **54**, 13379.

14 H.-R. Wen, J.-J. Hu, K. Yang, J.-L. Zhang, S.-J. Liu, J.-S. Liao and C.-M. Liu, Family of Chiral Zn^{II}-Ln^{III} (Ln = Dy and Tb) Heterometallic Complexes Derived from the Amine-Phenol Ligand Showing Multifunctional Properties, *Inorg. Chem.*, 2020, **59**, 2811.

15 C.-M. Liu, R. Sun, B.-W. Wang, X. Hao and X.-L. Li, Effects of Counterions, Coordination Anions, and Coordination Solvent Molecules on Single-Molecule Magnetic Behaviors and Nonlinear Optical Properties of Chiral Zn_2Dy Schiff Base Complexes, *Inorg. Chem.*, 2022, **61**, 18510.

16 X.-L. Li, A. Wang, M. Cui, C. Gao, X. Yu, B. Su, L. Zhou, C.-M. Liu, H.-P. Xiao and Y.-Q. Zhang, Modulating Two Pairs of Chiral Dy^{III} Enantiomers by Distinct β-Diketone Ligands to Show Giant Differences in Single-Ion Magnet Performance and Nonlinear Optical Response, *Inorg. Chem.*, 2022, **61**, 9283.

17 S.-D. Zhu, J.-J. Hu, L. Dong, H.-R. Wen, S.-J. Liu, Y.-B. Lu and C.-M. Liu, Multifunctional Zn(ii)–Yb(iii) complex enantiomers showing second-harmonic generation, near-infrared luminescence, single-molecule magnet behaviour and proton conduction, *J. Mater. Chem. C*, 2020, **8**, 16032.

18 B. E. Rez, J. Liu, V. Béreau, C. Duhayon, Y. Horino, T. Suzuki, L. Coolen and J.-P. Sutter, Concomitant emergence of circularly polarized luminescence and single-molecule magnet behavior in chiral-at-metal Dy complex, *Inorg. Chem. Front.*, 2020, **7**, 4527.

19 C. A. Mattei, V. Montigaud, F. Gendron, S. Denis-Quanquin, V. Dorcet, N. Giraud, F. Riobé, G. Argouarch, O. Maury, B. Le Guennic, O. Cador, C. Lalli and F. Pointillart, Solid-state versus solution investigation of a luminescent chiral BINOL-derived bisphosphate single-molecule magnet, *Inorg. Chem. Front.*, 2021, **8**, 947.

20 B. Lefeuvre, C. A. Mattei, J. F. Gonzalez, F. Gendron, V. Dorcet, F. Riobé, C. Lalli, B. Le Guennic, O. Cador, O. Maury, S. Guy, A. Bensalah-Ledoux, B. Baguenard and F. Pointillart, Solid-State Near-Infrared Circularly Polarized Luminescence from Chiral YbIII-Single-Molecule Magnet, *Chem. – Eur. J.*, 2021, **27**, 7362.

21 H. Huang, R. Sun, X.-F. Wu, Y. Liu, J.-Z. Zhan, B.-W. Wang and S. Gao, Circularly polarized luminescence and magneto-optic effects from chiral Dy(III) single molecule magnets, *Dalton Trans.*, 2023, **52**, 7646.

22 C. A. Mattei, V. Montigaud, B. Lefeuvre, V. Dorcet, G. Argouarch, O. Cador, B. Le Guennic, O. Maury, C. Lalli, Y. Guyot, S. Guy, C. Gindre, A. Bensalah-Ledoux, F. Riobé, B. Baguenard and F. Pointillart, Circularly polarized luminescence in the one-dimensional assembly of binaphtyl-based Yb(III) single-molecule magnets, *J. Mater. Chem. C*, 2023, **11**, 7299.

23 K. Wang, S. Zeng, H. Wang, J. Dou and J. Jiang, Magneto-chiral dichroism in chiral mixed (phthalocyaninato)(porphyrinato) rare earth triple-decker SMMs, *Inorg. Chem. Front.*, 2014, **1**, 167.

24 C.-M. Liu, R. Sun, B.-W. Wang, F. Wu, X. Hao and Z. Shen, Homochiral Ferromagnetic Coupling Dy_2 Single-Molecule Magnets with Strong Magneto-Optical Faraday Effects at Room Temperature, *Inorg. Chem.*, 2021, **60**, 12039.

25 X. Wang, M.-H. Du, H. Xu, L.-S. Long, X.-J. Kong and L.-S. Zheng, Cocrystallization of Chiral 3d-4f Clusters $\{Mn_{10}Ln_6\}$ and $\{Mn_6Ln_2\}$, *Inorg. Chem.*, 2021, **60**, 5925.

26 C.-M. Liu, S.-D. Zhu, Y.-B. Lu, X. Hao and H.-R. Wen, Homochiral Cu_6Dy_3 single-molecule magnets displaying proton conduction and a strong magneto-optical Faraday effect, *Inorg. Chem. Front.*, 2023, **10**, 3714.

27 C.-M. Liu, R. Sun, X. Hao and B.-W. Wang, Two Pairs of Homochiral Parallelogram-like Dy_4 Cluster Complexes with Strong Magneto-optical Properties, *Inorg. Chem.*, 2023, **62**, 20184.

28 M. S. Raju, K. Dhbaibi, M. Grasser, V. Dorcet, I. Breslavetz, K. Paillot, N. Vanthuyne, O. Cador, G. L. J. A. Rikken, B. Le Guennic, J. Crassous, F. Pointillart, C. Train and M. Atzori, Magneto-Chiral Dichroism in a One-Dimensional Assembly of Helical Dysprosium(III) Single-Molecule Magnets, *Inorg. Chem.*, 2023, **62**, 17583.

29 D. Gatteschi and R. Sessoli, Quantum Tunneling of Magnetization and Related Phenomena in Molecular Materials, *Angew. Chem., Int. Ed.*, 2003, **42**, 268.

30 C.-M. Liu, R.-G. Xiong, D.-Q. Zhang and D.-B. Zhu, Nanoscale Homochiral C_3-Symmetric Mixed-Valence Manganese Cluster Complexes with Both Ferromagnetic and Ferroelectric Properties, *J. Am. Chem. Soc.*, 2010, **132**, 4044.

31 L. Yao, Z. Zeng, C. Cai, P. Xu, H. Gu, L. Gao, J. Han, X. Zhang, X. Wang, X. Wang, A. Pan, J. Wang, W. Liang, S. Liu, C. Chen and J. Tang, Strong Second- and Third-Harmonic Generation in 1D Chiral Hybrid Bismuth Halides, *J. Am. Chem. Soc.*, 2021, **143**, 16095.

32 S.-T. Wang, X. Qi, R.-Q. Chen, W.-H. Fang and J. Zhang, Two solvent-dependent Al_{16} nanorings: design, synthesis and nonlinear optical limiting behavior, *Inorg. Chem. Front.*, 2024, **11**, 462.

33 Z. Wang, Y. Yan, J. Chen, Q.-H. Li and J. Zhang, Designed metal-organic π-clusters combining the aromaticity of the metal cluster and ligands for a third-order nonlinear optical response, *Mater. Horiz.*, 2024, **11**, 297.

34 L. He, P.-P. Shi, M.-M. Zhao, C.-M. Liu, W. Zhang and Q. Ye, Emergent Chirality and Nonlinear Optical Switching in a Ferroelastic Molecular Perovskite Solid Solution, *Chem. Mater.*, 2021, **33**, 799.

35 D. N. Woodruff, R. E. P. Winpenny and R. A. Layfield, Lanthanide Single-Molecule Magnets, *Chem. Rev.*, 2013, **113**, 5110.

36 Z. Zhu and J. Tang, Metal-metal bond in lanthanide single-molecule magnets, *Chem. Soc. Rev.*, 2022, **51**, 9469.

37 O. Cador, B. Le Guennic and F. Pointillart, Electro-activity and magnetic switching in lanthanide-based single-molecule magnets, *Inorg. Chem. Front.*, 2022, **9**, 6061.

38 C. A. P. Goodwin, F. Ortu, D. Reta, N. F. Chilton and D. P. Mills, Molecular Magnetic Hysteresis at 60 Kelvin in Dysprosocenium, *Nature*, 2017, **548**, 439.

39 F.-S. Guo, B. M. Day, Y.-C. Chen, M.-L. Tong, A. Mansikkamäki and R. A. Layfield, Magnetic hysteresis up to 80 kelvin in a dysprosium metallocene single-molecule magnet, *Science*, 2018, **362**, 1400.

40 J. Liu, Y.-C. Chen, J.-L. Liu, V. Vieru, L. Ungur, J.-H. Jia, L. F. Chibotaru, Y. Lan, W. Wernsdorfer, S. Gao,

X.-M. Chen and M.-L. Tong, A Stable Pentagonal Bipyramidal Dy(III) Single-Ion Magnet with a Record Magnetization Reversal Barrier over 1000 K, *J. Am. Chem. Soc.*, 2016, **138**, 5441.

41 Y.-S. Ding, N. F. Chilton, R. E. P. Winpenny and Y.-Z. Zheng, On Approaching the Limit of Molecular Magnetic Anisotropy: A Near-Perfect Pentagonal Bipyramidal Dysprosium(III) Single-Molecule Magnet, *Angew. Chem., Int. Ed.*, 2016, **55**, 16071.

42 R. Sun, C. Wang, B.-W. Wang, Z.-M. Wang, Y.-F. Chen, M. Tamm and S. Gao, Low-coordinate bis(imidazolin-2-iminato) dysprosium(III) single-molecule magnets, *Inorg. Chem. Front.*, 2023, **10**, 485.

43 Y.-S. Meng, S.-D. Jiang, B.-W. Wang and S. Gao, Understanding the Magnetic Anisotropy toward Single-Ion Magnets, *Acc. Chem. Res.*, 2016, **49**, 2381.

44 Y. Kitagawa, S. Wada, K. Yanagisawa, T. Nakanishi, K. Fushimi and Y. Hasegawa, Molecular Design Guidelines for Large Magnetic Circular Dichroism Intensities in Lanthanide Complexes, *ChemPhysChem*, 2016, **17**, 845.

45 H. Tian, L. Ungur, L. Zhao, S. Ding, J. Tang and L. F. Chibotaru, Exchange Interactions Switch Tunneling: A Comparative Experimental and Theoretical Study on Relaxation Dynamics by Targeted Metal Ion Replacement, *Chem. – Eur. J.*, 2013, **19**, 8769.

46 Y.-N. Guo, G.-F. Xu, W. Wernsdorfer, L. Ungur, Y. Guo, J. Tang, H.-J. Zhang, L. F. Chibotaru and A. K. Powel, Strong Axiality and Ising Exchange Interaction Suppress Zero-Field Tunneling of Magnetization of an Asymmetric Dy_2 Single-Molecule Magnet, *J. Am. Chem. Soc.*, 2011, **133**, 11948.

47 H. Tian, B.-L. Wang, J. Lu, H.-T. Liu, J. Su, D. Li and J. Dou, Consecutive one-/two-step relaxation transformations of single-molecule magnets via coupling dinuclear dysprosium compounds with chloride bridges, *Chem. Commun.*, 2018, **54**, 12105.

48 Y.-N. Guo, X.-H. Chen, S. Xue and J. Tang, Modulating Magnetic Dynamics of Three Dy_2 Complexes through Keto–Enol Tautomerism of the o-Vanillin Picolinoylhydrazone Ligand, *Inorg. Chem.*, 2011, **50**, 9705.

49 Y. Jiang, G. Brunet, R. J. Holmberg, F. Habib, I. Korobkov and M. Murugesu, Terminal solvent effects on the anisotropy barriers of Dy_2 systems, *Dalton Trans.*, 2016, **45**, 16709.

50 X.-M. Zhang, Y.-Y. Duan, H.-L. Gao and J.-Z. Cui, Solvent-induced single-molecule magnet behavior and near-infrared luminescence properties of rare earth complexes, *New J. Chem.*, 2020, **44**, 19135.

51 D. Casanova, M. Llunell, P. Alemany and S. Alvarez, The Rich Stereochemistry of Eight-Vertex Polyhedra: a Continuous Shape Measures Study, *Chem. – Eur. J.*, 2005, **11**, 1479.

52 C.-M. Liu, X. Hao, D.-M. Zhu and Y.-Q. Zhang, Effect of coordinated anions on ferromagnetically coupled Dy_2 zero-field single-molecule magnets, *Dalton Trans.*, 2024, **53**, 6120.

53 K. S. Cole and R. H. Cole, Dispersion and Absorption in Dielectrics I. Alternating Current Characteristics, *J. Chem. Phys.*, 1941, **9**, 341.

54 S. M. Aubin, Z. Sun, L. Pardi, J. Krzysteck, K. Folting, L.-J. Brunel, A. L. Rheingold, G. Christou and D. N. Hendrickson, Reduced Anionic Mn_{12} Molecules with Half-Integer Ground States as Single-Molecule Magnets, *Inorg. Chem.*, 1999, **38**, 5329.

55 Y.-N. Guo, G.-F. Xu, P. Gamez, L. Zhao, S.-Y. Lin, R. Deng, J. Tang and H.-J. Zhang, Two-Step Relaxation in a Linear Tetranuclear Dysprosium(III) Aggregate Showing Single-Molecule Magnet Behavior, *J. Am. Chem. Soc.*, 2010, **132**, 8538.

56 C.-M. Liu, D.-Q. Zhang and D.-B. Zhu, A single-molecule magnet featuring a parallelogram $[Dy_4(OCH_2^-)_4]$ core and two magnetic relaxation processes, *Dalton Trans.*, 2013, **42**, 14813.

57 S. K. Langley, N. F. Chilton, B. Moubaraki and K. S. Murray, Single-Molecule Magnetism in Three Related $\{Co^{III}{}_2Dy^{III}{}_2\}$-Acetylacetonate Complexes with Multiple Relaxation Mechanisms, *Inorg. Chem.*, 2013, **52**, 7183.

58 L. F. Chibotaru, L. Ungur and A. Soncini, Origin of non-magnetic Kramers doublets in the ground state of dysprosium triangles: Evidence for toroidal magnetic moment, *Angew. Chem., Int. Ed.*, 2008, **47**, 4126.

59 L. F. Chibotaru, L. Ungur, C. Aronica, H. Elmoll, G. Pilet and D. Luneau, Structure, magnetism and theoretical study of mixed-valent $Co^{II}{}_3Co^{III}{}_4$ heptanuclear wheel: Lack of SMM behaviour despite negative magnetic anisotropy, *J. Am. Chem. Soc.*, 2008, **130**, 12445.

60 F. Aquilante, J. Autschbach, R. K. Carlson, L. F. Chibotaru, M. G. Delcey, L. D. Vico, I. F. Galván, N. Ferré, L. M. Frutos, L. Gagliardi, M. Garavelli, A. Giussani, C. E. Hoyer, G. L. Manni, H. Lischka, D. Ma, P. Å. Malmqvist, T. Müller, A. Nenov, M. Olivucci, T. B. Pedersen, D. Peng, F. Plasser, B. Pritchard, M. Reiher, I. Rivalta, I. Schapiro, J. Segarra-Martí, M. Stenrup, D. G. Truhlar, L. Ungur, A. Valentini, S. Vancoillie, V. Veryazov, V. P. Vysotskiy, O. Weingart, F. Zapata and R. Lindh, Molcas 8: New capabilities for multiconfigurational quantum chemical calculations across the periodic table, *J. Comput. Chem.*, 2016, **37**, 506.

61 M. E. Lines, Orbital Angular Momentum in the Theory of Paramagnetic Clusters, *J. Chem. Phys.*, 1971, **55**, 2977.

62 G. L. J. A. Rikken and E. Raupach, Enantioselective magnetochiral photochemistry, *Nature*, 2000, **405**, 932.

63 G. L. J. A. Rikken and E. Raupach, Observation of magneto-chiral dichroism, *Nature*, 1997, **390**, 493.

64 X. Zhang, L. Kang, P. Gong, Z. Lin and Y. Wu, Nonlinear Optical Oxythiophosphate Approaching the Good Balance with Wide Ultraviolet Transparency, Strong Second Harmonic Effect, and Large Birefringence, *Angew. Chem., Int. Ed.*, 2021, **60**, 6386.

65 C. Bosshard, U. Gubler, P. Kaatz, W. Mazerant and U. Meier, Non-phase-matched optical third-harmonic generation in noncentrosymmetric media: Cascaded second-order contributions for the calibration of third-order nonli-

nearities, *Phys. Rev. B: Condens. Matter Mater. Phys.*, 2000, **61**, 10688.

66 M. Cui, L. Yang, F. Li, L. Zhou, Y. Song, S.-M. Fang, C.-M. Liu and X.-L. Li, Multifunctional Dy^{III} Enantiomeric Pairs Showing Enhanced Photoluminescences and Third-Harmonic Generation Responses through the Coordination Role of Homochiral Tridentate N,N,N-Pincer Ligands, *Inorg. Chem.*, 2021, **60**, 13366.

67 J. Liang, J. Wang, Z. Zhang, Y. Su, Y. Guo, R. Qiao, P. Song, P. Gao, Y. Zhao, Q. Jiao, S. Wu, Z. Sun, D. Yu and K. Liu, Universal Imaging of Full Strain Tensor in 2D Crystals with Third-Harmonic Generation, *Adv. Mater.*, 2019, **31**, 1808160.